

ARTICLE OPEN

Dilute carbon in H₃S under pressureXiaoyu Wang¹, Tiange Bi¹, Katerina P. Hilleke¹, Anmol Lamichhane², Russell J. Hemley³✉ and Eva Zurek¹✉

Recently, room temperature superconductivity was measured in a carbonaceous sulfur hydride material whose identity remains unknown. Herein, first-principles calculations are performed to provide a chemical basis for structural candidates derived by doping H₃S with low levels of carbon. Pressure stabilizes unusual bonding configurations about the carbon atoms, which can be six-fold coordinated as CH₆ entities within the cubic H₃S framework, or four-fold coordinated as methane intercalated into the H-S lattice, with or without an additional hydrogen in the framework. The doping breaks degenerate bands, lowering the density of states at the Fermi level (N_F), and localizing electrons in C-H bonds. Low levels of CH₄ doping do not increase N_F to values as high as those calculated for $Im\bar{3}m$ -H₃S, but they can yield a larger logarithmic average phonon frequency, and an electron–phonon coupling parameter comparable to that of $R3m$ -H₃S. The implications of carbon doping on the superconducting properties are discussed.

npj Computational Materials (2022)8:87; <https://doi.org/10.1038/s41524-022-00769-9>

INTRODUCTION

The decades old quest for a near room-temperature superconductor has recently come to fruition. Inspired by Ashcroft's predictions that hydrogen-rich compounds metallized under pressure could be phonon-mediated high-temperature superconductors^{1,2}, synergy between experiment and theory has led to remarkable progress^{3–5}. A superconducting critical temperature, T_c , of 203 K near 150 GPa was reported for H₃S⁶, followed by a T_c of 260 K near 200 GPa in LaH₁₀^{7,8}. Later, a carbonaceous sulfur hydride superconductor with a T_c of 288 K at 267 GPa was reported⁹. Many questions remain unanswered about this system; perhaps the most pressing being: "What is the composition and structure of the phase, or phases, responsible for the remarkable superconductivity?" Recent x-ray diffraction (XRD) studies suggest the material is derived from the Al₂Cu structure type up to 180 GPa^{10–12}, but its evolution upon further compression where the T_c is highest has not yet been determined experimentally. The reported T_c versus pressure⁹ shows evidence for a transition near 200 GPa, although the scatter in the data are consistent with a continuous change in T_c . On the other hand, the XRD results suggest that this change in T_c could arise from the collapse of the observed lower symmetry orthorhombic to higher symmetry superconducting phases¹¹. Moreover, recent studies of the C-S-H system suggest a T_c as high as 191 K near 100 GPa, results that highlight the sensitivity of the material to the thermodynamic paths used to synthesize the high T_c phase.¹³

To understand the nature of carbonaceous sulfur hydride, it is useful to review the work leading to the discovery of the initial high- T_c H₃S superconductor¹⁴. Synthesis of (H₂S)₂H₂ van der Waals compounds at pressures up to 40 GPa¹⁵ inspired the computational search for additional H-S phases that might be stable and potentially superconducting at megabar pressures^{16,17}. An $Im\bar{3}m$ symmetry H₃S phase, which can be described as a body centered cubic sulfur lattice with H atoms lying midway between adjacent S atoms ($T_c = 191–204$ K at 200 GPa), was predicted to be stable above 180 GPa. An analogous lower-symmetry $R3m$ phase with asymmetric H-S bonds was preferred at pressures down to 110 GPa ($T_c = 155–166$ K at 130 GPa)¹⁷. Experiments on the H-S system confirmed the maximum T_c (203 K) near the expected

pressures (155 GPa), leading to the proposal that the synthesized structure was the predicted $Im\bar{3}m$ phase⁶. Subsequently XRD measurements largely confirmed the predicted cubic structure^{18,19}. However, the synthesis conditions were found to dictate the product that formed, and T_c s as low as 33 K were measured. Thus, reproducing the synthesis of the cubic phase proved difficult^{20,21}, and more recently altogether new structures have been reported²².

These observations suggest that a number of H_xS_y superconductors can be made. Indeed, additional peaks observed in XRD measurements have been assigned to possible secondary phases^{18,21}. Various stoichiometries including H₂S^{16,23}, HS₂²⁴, H₄S₃²⁵, and H₅S₂²⁶ have been proposed for materials with lower T_c s. Exotic Magnéli phases with H_xS_{1–x}} (2/3 < x < 3/4) compositions characterized by alternating H₂S and H₃S regions with a long modulation whose ratio can be varied to tune the T_c have also been proposed²⁷. First-principles calculations suggested that H₂S self-ionizes under pressure forming a (SH[–])(H₃S)⁺ perovskite-type structure²⁸ that may undergo further deformations to a complex modulated phase^{29,30}. A $Z = 24$ $R\bar{3}m$ symmetry phase whose density of states (DOS) at the Fermi level (E_F) was predicted to be lower than that of $R3m$ and $Im\bar{3}m$ H₃S was computed to be more stable than these two phases between 110 and 165 GPa³¹. The role of quantum nuclear and anharmonic effects on the $R3m \rightarrow Im\bar{3}m$ transition and T_c has been investigated^{32,33}, as has the response of the Fermi surface to uniaxial strain³⁴.

Turning to the C-S-H ternary, initial crystal structure prediction calculations conducted prior to the discovery of the carbonaceous sulfur hydride superconductor considered stoichiometric C_xS_yH_z compositions with relatively high carbon dopings^{35,36}. These studies identified metastable CSH₇ structures that were based on the intercalation of methane into an H₃S framework, with maximum T_c s estimated to be 194 K at 150 GPa³⁵ and 181 K at 100 GPa³⁶. Since then other stoichiometries based on these structural motifs, such as CS₂H₁₀, have been explored^{37,38}. However, the measured structural parameters, P – V equations of state¹¹, and the variation of T_c versus pressure⁹ do not match those calculated for these hydride perovskite-like materials. First-principles calculations employing the virtual crystal approximation (VCA) predicted that remarkably low-level hole-doping resulting

¹Department of Chemistry, State University of New York at Buffalo, Buffalo, NY, USA. ²Department of Physics, University of Illinois Chicago, Chicago, IL, USA. ³Departments of Physics, Chemistry, and Earth and Environmental Sciences, University of Illinois Chicago, Chicago, USA. ✉email: rhemley@uic.edu; ezurek@buffalo.edu

from the incorporation of carbon in the parent H_3S phase (i.e. $\text{C}_{0.038}\text{S}_{0.962}\text{H}_3$) could increase the T_c up to 288 K³⁹. It was argued that doping tunes the position of E_F , moving it closer to the maximum in the DOS that arises from the presence of two van Hove singularities (vHs). Because vHs increase the number of states that can participate in the electron-phonon-coupling (EPC) mechanism, this effect is known in general to enhance the total coupling strength, λ , and in turn the T_c in conventional superconductors. The role that the vHs play in increasing the T_c in H_3S has been studied in detail^{40–43}.

Despite the striking success of the VCA model in reproducing theoretically the very high T_c measured for the C–S–H superconductor³⁹, this approach does not take into account the effect of the doping on the local structure and electronic properties, and its limitations have been discussed^{44,45}. To overcome these limitations we systematically study the role of doping on the thermodynamic and dynamic stability, electronic structure, and geometric properties of phases with doping levels as low as 1.85%. Three types of substitutions are considered involving S replaced by C, together with different numbers of hydrogens, yielding either six-fold or four-fold coordinate carbon atoms. We find that CH_6 and CH_4 form stable configurations within the dense solid in phases that are dynamically stable at the pressures studied experimentally. Moreover, doping *decreases* the DOS at E_F because it breaks degeneracies and localizes electrons in C–H bonds. Our results illustrate that the rigid band model does not reliably predict the superconducting properties of the doped phases. Finally, the descriptors associated with superconductivity, such as

the DOS at E_F , the logarithmic averaged phonon frequency, and T_c of various metastable C–S–H phases are analyzed.

RESULTS AND DISCUSSION

Octahedrally coordinated carbon in $\text{C}_x\text{S}_{1-x}\text{H}_3$ phases

To investigate how different levels of doping affect the kinetic and thermodynamic stability, electronic structure, and superconducting properties of H_3S , we constructed supercells of the $Im\bar{3}m$ structure where one of the sulfur atoms was replaced by carbon. Calculations were carried out at 270 GPa with $\text{C}_x\text{S}_{1-x}\text{H}_3$ stoichiometries and two different types of coordination environments around the dopant atom were considered. In the first type the carbon atom was octahedrally coordinated by six hydrogen atoms, and in the second type two of these C–H bonds broke resulting in a quasi-tetrahedral CH_4 molecule. A detailed analysis was carried out on the $\text{C}_{0.0625}\text{S}_{0.9375}\text{H}_3$ ($\text{CS}_{15}\text{H}_{48}$) stoichiometry at 270 GPa, which was dynamically stable for both carbon coordination environments (as illustrated in Supplementary Figs. 2f and 8c).

The calculated C–H distance in the octahedrally coordinated phase, which we refer to as $O_h\text{-CS}_{15}\text{H}_{48}$ (Fig. 1a), measures 1.17 Å. The negative of the crystal orbital Hamilton population integrated to the Fermi level (-iCOHP), which can be used to quantify the bond strength, is calculated to be 5.11 eV for this bond. The distance between the hydrogen atom bonded to carbon and its nearest neighbor sulfur (1.71 Å), is significantly larger than the H–S distance found in $Im\bar{3}m$ H_3S at this pressure (1.45 Å). The weakening of the CH–S bond upon doping is evident in

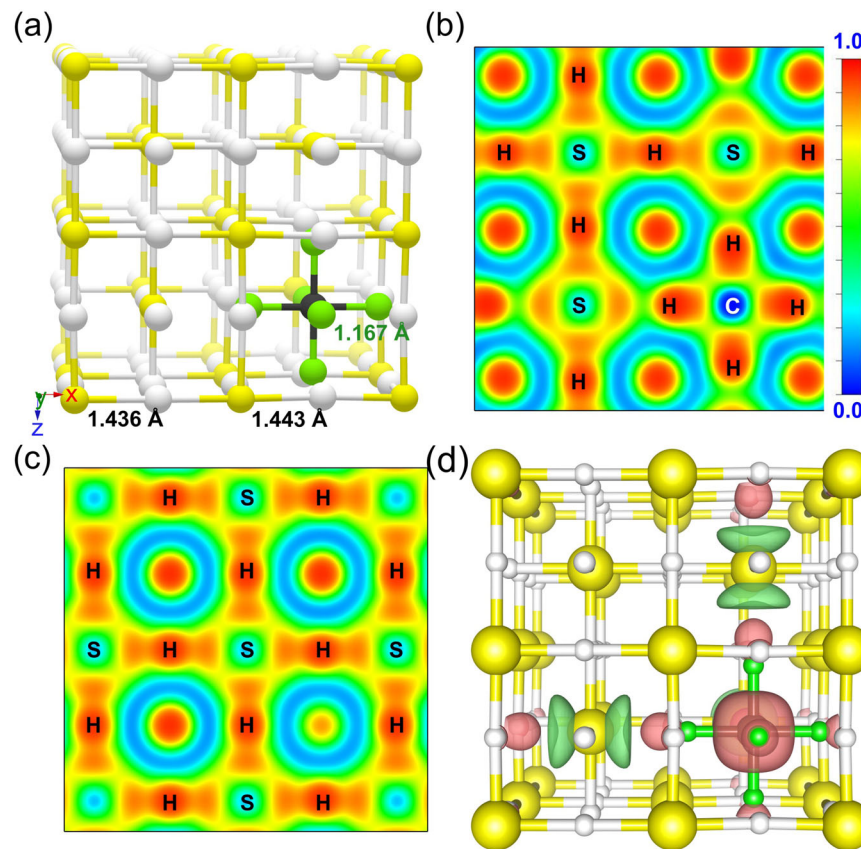


Fig. 1 Geometry and electronic structure of $O_h\text{-CS}_{15}\text{H}_{48}$. **a** Optimized geometry and **b**, **c** electron localization function (ELF) contour plot of $\text{C}_{0.0625}\text{S}_{0.9375}\text{H}_3$ ($O_h\text{-CS}_{15}\text{H}_{48}$, space group $Pm\bar{3}m$), where the carbon atom is octahedrally coordinated by hydrogen atoms at 270 GPa. The plane of the contour passes through **b** CH_6 and **c** H_3S , and the range of the isovalues is from 0.0 (blue/cold) to 1.0 (red/warm). The atoms through which the plane passes are labelled. **d** The following electron density difference: $\rho(\text{CH}_6) + \rho(\text{S}_{15}\text{H}_{42}) - \rho(\text{CS}_{15}\text{H}_{48})$ where red denotes a loss of charge and green a gain of charge (isovalue = 0.005). Sulfur/carbon/hydrogen atoms are yellow/black/white and select geometric parameters are provided. Hydrogen bonded to carbon is green.

the $-i\text{COHP}$, which decreases from 3.74 eV/bond (in H_3S) to 2.00 eV/bond. Despite the non-negligible $-i\text{COHPs}$ between the hydrogen atoms bonded to carbon and the nearest neighbor sulfur atoms, the ELF (Fig. 1b) does not show any evidence of covalent CH–S bond formation. The integrated crystal orbital bond index (iCOBI), which is a quantification of the extent of covalent bond formation⁴⁶, is calculated to be 0.34 for each S–H bond in H_3S , indicating a bond order of roughly 1/3. Substituting C in an octahedral coordination environment leaves the S–H iCOBI essentially unchanged for bonds distant from the C substitution site, but for CH–S bonds the iCOBI drops to 0.21, showing the weakening of this bond. Practically no antibonding states are filled in the S–H interaction with H coordinating C (Supplementary Discussion 1), but the increased S–H distance leads to an overall decrease in the magnitude of the iCOBI. The C–H bonds in the octahedral CH_6 motif possess the largest iCOBI in the system, 0.51. Subtracting the charge density of the $\text{CS}_{15}\text{H}_{48}$ structure from a sum of the density arising from the neutral CH_6 molecule and the neutral H–S framework (Fig. 1d) illustrates that charge is transferred from the CH_6 unit into the nearest neighbor sulfur lone pairs, which can also be seen in the ELF plot (Fig. 1b). A Bader analysis, which typically underestimates the formal charge, yields a +0.25 charge on CH_6 , indicating that charge redistribution is associated with stabilization of this configuration in the dense structure.

An analysis using the reversed approximation Molecular Orbital (raMO) method⁴⁷, which uses linear combinations of the occupied crystal orbitals of the system to reproduce target orbitals, revealed substantial bonding interactions within the CH_6 cluster. The reproduced s orbital on the hydrogen atom in this motif contained electron density with p -orbital symmetry on the neighboring C atom, indicative of sp bonding. Similarly, the reproduced s orbital on C strongly interacted with the surrounding H atoms, which is evident in its anisotropy as compared to the more isotropic sulfur s orbital reproductions (Supplementary Discussion 2).

Theoretical considerations have been key in designing ways to stabilize four-coordinate carbon in unusual bonding configurations such as planar tetracoordinate carbon^{48,49}. While a wide variety of molecular compounds containing coordination numbers surpassing four, such as carbocations, carboranes, organometallics, and carbon clusters, are also known^{50,51}, octahedrally coordinated carbon is quite unusual. Examples include elemental carbon, which has been predicted to become six-fold coordinate at terapascal pressures^{52,53}, and high pressure Si–C compounds such as rock-salt $\text{SiC}^{54,55}$, and two predicted Si_3C phases⁵⁶. More relevant to the C–S–H system are carbon atoms bonded to more

than four hydrogen atoms such as the nonclassical carbocation, $\text{C}_5\text{-CH}_5^+$, which contains three short and two long C–H bonds. It can be viewed as a proton inserted into one of the σ C–H bonds within methane, forming a three-center two-electron ($3c\text{-}2e$) bond between one carbon and two hydrogen atoms⁵⁷. Ab initio calculations for the isolated molecule have shown that the minimum energy configuration for the di-carbocation, CH_6^{2+} , possesses C_{2v} symmetry with two long $3c\text{-}2e$ and two short classic $2c\text{-}2e$ bonds, rather than the O_h symmetry CH_6^{2+} geometry^{58,59}. Following one of the triply degenerate imaginary normal modes, which can be described as a wagging motion along the three sets of H–C–H 180° angles in the octahedron, leads to the C_{2v} minimum. Turning now to the hypercoordinated carbon atom in the $O_h\text{-CS}_{15}\text{H}_{48}$ model structure, explicit calculation of the phonons at the Γ point reveals that in the solid state the frequency of this same triply degenerate mode is real (calculated frequency of 1712 cm^{-1}), and the vibration is coupled with the motions of the hydrogens in the H_3S lattice. Thus, the stabilization of the octahedral molecular complex is facilitated by weak interactions with the host lattice. Notably, the calculated C–H bond length in CH_6^{2+} obtained at the HF/6-311+G(2d,p) level of theory, is nearly identical to that of $O_h\text{-CS}_{15}\text{H}_{48}$ at 270 GPa (both $\sim 1.17\text{ \AA}$). That the carbon weakly interacts with the host lattice is supported by calculations where the carbon (or sulfur) is replaced with neon. The optimized $O_h\text{-NeS}_{15}\text{H}_{48}$ structure is dynamically stable at these pressures, with a calculated Ne–H distance of 1.37 \AA (Supplementary Fig. 27).

Quasi-tetrahedrally coordinated carbon in $\text{C}_x\text{S}_{1-x}\text{H}_3$ phases

When placed in a cube a tetrahedral methane molecule can retain its symmetry only if its hydrogens point toward four corners of the cube. In the phases studied here such an orientation introduces unfavorable steric interactions, and a lower enthalpy can be obtained when the hydrogens point towards four cube faces instead. Because of this the four coordinate CH_4 species within the phase we refer to as $T_d\text{-CS}_{15}\text{H}_{48}$ actually possesses C_{2v} symmetry. As illustrated in Fig. 2a, at 270 GPa its two C–H bond lengths are nearly identical with calculated $-i\text{COHPs}$ of 6.34 and 6.30 eV/bond. The H–S distances between two of the hydrogens bonded to carbon elongate to 1.73 \AA , and a further two to 1.91 \AA . At the same time two of the S–H bonds contract relative to those within $Im\bar{3}m$ H_3S (1.35 \AA). The encapsulated methane molecule possesses H–C–H angles that deviate from the ideal tetrahedral angle (100° , 103° , and 140°), and its Bader charge, -0.09 , is suggestive of electron donation from the H–S lattice. Plots of the

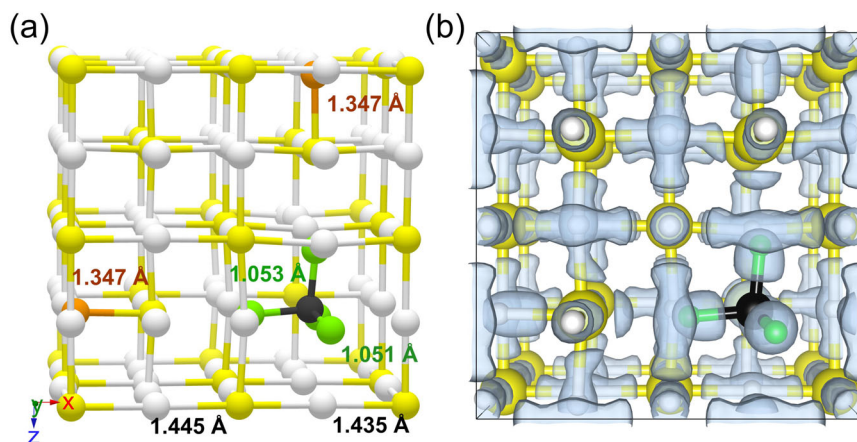


Fig. 2 Geometry and electronic structure of $T_d\text{-CS}_{15}\text{H}_{48}$. **a** Optimized geometry and **b** electron localization function (ELF; isovalue = 0.8) of the CH_4 -based $\text{C}_{0.0625}\text{S}_{0.9375}\text{H}_3$ ($T_d\text{-CS}_{15}\text{H}_{48}$, space group $Amm2$) in which the carbon atom is quasi-tetrahedrally coordinated by hydrogen atoms at 270 GPa. Sulfur/carbon/hydrogen atoms are yellow/black/white and select geometric parameters are provided. Hydrogens bonded to carbon/sulfur only are green/orange. ELF contour plot is provided in Supplementary Fig. 19.

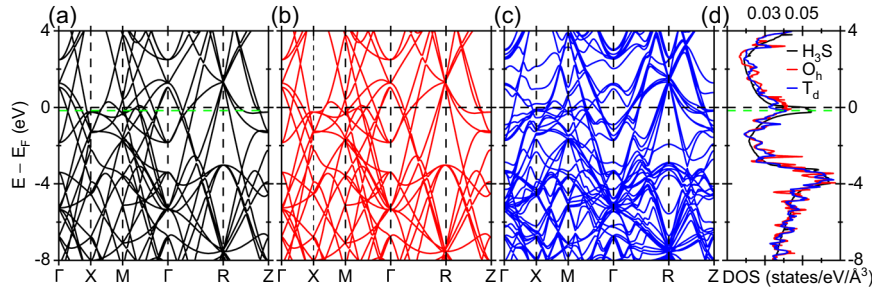


Fig. 3 Band structure and density of states at 270 GPa. **a** $Im\bar{3}m$ H_3S in a $2 \times 2 \times 2$ supercell of the standard conventional lattice, **b** $Pm\bar{3}m$ O_h - $CS_{15}H_{48}$, and **c** $Amm2$ T_d - $CS_{15}H_{48}$. To compare the band structures of the three phases, which all possess different space-groups, simple cubic symmetry is assumed and the high symmetry special points used are Γ (0,0,0), X (0.5,0,0), M (0.5,0.5,0) and R (0.5,0.5,0.5). **d** Densities of states of these phases where O_h denotes $CS_{15}H_{48}$ with hexacoordinate carbon and T_d with tetra-coordinate carbon. The black horizontal dashed line denotes E_F and the green dashed line $E_F - 0.17$ eV, which corresponds to the top of the peak in the DOS in $Im\bar{3}m$ H_3S .

ELF (Fig. 2b) clearly illustrate the C–H bond, but do not show any evidence of covalent bond formation between CH_4 and the H–S framework. Thus, two H–S and four C–H bonds per unit cell in T_d - $CS_{15}H_{48}$ become classical 2c–2e bonds, no longer participating in delocalized multi-centered bonding as they would within H_3S .

Properties of the S \rightarrow C Doped Phases at 270 GPa

Our calculations find the DOS at the Fermi level, N_F , in H_3S to be 0.050 states $eV^{-1} \text{ \AA}^{-3}$ at 270 GPa. Moving E_F down in energy by 0.17 eV, which can be achieved by doping with $\sim 5.7\%$ C, yields the highest possible value of 0.055 states $eV^{-1} \text{ \AA}^{-3}$. Given a reference material whose superconducting critical temperature, T_c^0 , is known, the approximate Bardeen–Cooper–Schrieffer formula can be employed to estimate the T_c of a similar material via the formula $T_c = 1.13\Theta_D(T_c^0/1.13\Theta_D)^{N_c^0/N_F}$, where Θ_D is the Debye temperature and N_F is given per unit volume⁶⁰. Using the measured value of $T_c^0 = 170$ K at 270 GPa for $Im\bar{3}m$ H_3S ¹⁹, this simple model, which neglects the likely increase of λ that is associated with an increase in the DOS at E_F , predicts a T_c of 208 K for $\sim 5.7\%$ C doping, which is somewhat lower than the results obtained using the VCA at the same pressure and doping level³⁹.

To study the effect of doping on the electronic structure, we performed a single point calculation on an unrelaxed $2 \times 2 \times 2$ supercell of $Im\bar{3}m$ H_3S where a single sulfur atom was replaced by carbon. In contrast to the VCA model predictions we found that N_F decreases to 0.048 states $eV^{-1} \text{ \AA}^{-3}$. Structural relaxation to the O_h - and T_d - $CS_{15}H_{48}$ phases further lowers N_F to 0.040 and 0.033 states $eV^{-1} \text{ \AA}^{-3}$, respectively, as illustrated in Fig. 3. This initially counter-intuitive behavior of N_F can be understood by considering the following: replacing sulfur by carbon followed by structural relaxation decreases the number of degenerate bands near E_F because some of the metallic electrons that were delocalized in the H_3S framework now become localized in covalent C–H bonds. Whereas 14 bands (some of which are degenerate) cross $E_F - 0.17$ eV in $Im\bar{3}m$ H_3S at 270 GPa, only 11 bands intersect with the Fermi level within both O_h - and T_d - $CS_{15}H_{48}$ (Fig. 3a–c).

We also investigated how the vibrational properties of $Im\bar{3}m$ H_3S are affected by carbon doping. The Θ_D of the phase where carbon is four-coordinate is larger than that containing six-coordinate carbon, which is higher than that of pure H_3S (Table 1). The highest vibrational modes in T_d - $CS_{15}H_{48}$ corresponded to the asymmetric (~ 3125 and 3290 cm^{-1}), and symmetric H–C–H stretch (~ 3140 and 3170 cm^{-1}). O_h - $CS_{15}H_{48}$ possessed a high frequency C–H stretching mode at ~ 2360 cm^{-1} . Because the quasi-molecular CH_4 species possesses stronger and shorter C–H bonds as compared to the octahedrally coordinated carbon, these vibrations are found at higher frequencies.

$C_xS_{1-x}H_3$ phases as a function of doping and pressure

We now consider the dynamic stability of the $C_xS_{1-x}H_3$ stoichiometries as a function of doping at 270 GPa, beginning with phases where carbon is octahedrally coordinated. Both the H–S and H–C bond lengths in the 50% doped dynamically unstable CSH_6 structure measured 1.37 \AA . A majority of the phonon modes that were imaginary at some point within the Brillouin zone turned out to be related to the motions of the hydrogen atoms bonded to carbon. Decreasing the doping level to 25% allowed the C–H and S–H bonds to assume different lengths so that some of the imaginary modes in the 50% doped structure became real, specifically the asymmetric and symmetric H–C–H stretching modes.

For 25 (12.5%) doping a structure with $P4/mmm$ symmetry was found to be 78 (18) meV/atom less stable than one with $Fm\bar{3}m$ ($Im\bar{3}m$) symmetry. The dynamic instability in $P4/mmm$ CS_3S_{12} was associated with the movement of a hydrogen atom sandwiched between two carbons resulting in the lengthening of one, and contraction of another C–H bond that measured 1.41 \AA . In $Fm\bar{3}m$ CS_3S_{12} such C–H–C contacts are absent, but a mode emerges around 2345 cm^{-1} corresponding to the symmetric H–C–H stretching mode where the C–H bonds measure 1.17 \AA . However, the asymmetric H–C–H stretching modes, which are triply degenerate at Γ , are imaginary. They are coupled with the motion of an isolated S atom (S–H distances of 1.65 \AA) that attempts to achieve higher coordination and form CH–S bonds. The 12.5% doped $P4/mmm$ phase is dynamically unstable as well, but in $Im\bar{3}m$ CS_3S_{24} C–H–C contacts are absent, while the S atoms that are undercoordinated in the 25% doped structure are all stabilized by the formation of S–H–S motifs. The symmetric H–C–H stretch is at ~ 2350 cm^{-1} with a C–H bond length of 1.17 \AA , while the asymmetric stretch, which is coupled to the asymmetric H–S–H stretch, appears at ~ 1980 cm^{-1} . At ~ 1850 cm^{-1} a symmetric scissoring H–C–H mode appears. This phase becomes dynamically stable above 260 GPa.

$CS_{15}H_{48}$, which was dynamically stable between 255 and 270 GPa (Supplementary Fig. 4), was also considered. In it, the carbon atoms were far enough apart to prevent the formation of unstable environments such as C–H–C bonds or undercoordinated S atoms. At 240 GPa visualization of one of the triply degenerate imaginary modes at Γ revealed that it can be described as a lengthening/contraction of the CH–S distance, which measured 1.73 \AA in the optimized structure, with the other two modes corresponding to the same vibration but along the other crystallographic axes. Upon decreasing pressure from 270 to 240 GPa the C–H bond length increased minimally ($\Delta d = 0.005$ \AA , $-\Delta iCOHP = 0.02$ eV/bond), whereas the increase in the CH–S distance was an order of magnitude larger ($\Delta d = 0.03$ \AA , $-\Delta iCOHP = 0.10$ eV/bond). These results suggest that the instability that emerges near

Table 1. Electronic, vibrational, and superconducting properties of dynamically stable phases at 270 GPa.

Structure	Θ_D	N_F	ω_{in}	λ	T_c^{ME}	T_c^{AD}	P_{stab}
$Im\bar{3}m$ H ₃ S	1288	0.050	1626	1.24	175–162	166–148	N/A
$R3m$ H ₃ S	1330	0.044	1652	1.02	135–115	125–107	N/A
$Im\bar{3}m$	1366	0.030					260–270
O_h -CS ₇ H ₂₄							
$Pm\bar{3}m$	1382	0.040					255–270
O_h -CS ₁₅ H ₄₈							
$Pm\bar{3}m$	1368	0.048					200–270
O_h -CS ₅₃ H ₁₆₂							
$Amm2$	1752	0.028	1370	0.85	80–67	76–63	160–270
T_d -CS ₃ H ₁₂							
$Amm2$	1824	0.039					250–270
T_d -CS ₇ H ₂₄							
$Fmm2$	1525	0.039					200–270
T_d -CS ₇ H ₂₄							
Pm	1701	0.033					140–270
T_d -CS ₇ H ₂₄							
$Amm2$	1623	0.033					180–270
T_d -CS ₁₅ H ₄₈							
$Amm2$	1678	0.046					200–270
T_d -CS ₅₃ H ₁₆₂							
$Cmcm$ CSH ₇	1821	0.026					140–270
$R3m$ CSH ₇	1780	0.028	1703	1.10	156–140	147–129	140–270
Cm CS ₃ H ₁₃	1810	0.025	1704	1.01	142–121	128–110	140–270
$R3m$ CS ₃ H ₁₃	1664	0.028	1250	1.02	111–98	96–83	140–270
Cm CS ₇ H ₂₅	1832	0.031	1551	0.94	115–100	104–88	140–270
$R3m$ CS ₇ H ₂₅	1729	0.038					160–270
$R3m$ CS ₁₅ H ₄₉	1760	0.034					140–270
$R3m$	1792	0.043					200–270
CS ₅₃ H ₁₆₃							

Debye temperature (Θ_D , in K), density of states at the Fermi level (N_F , in states $eV^{-1}A^{-3}$), logarithmic average of phonon frequencies (ω_{in} , in K), electron-phonon coupling constant (λ), and superconducting critical temperature (T_c , in K) obtained via numerical solution of the Migdal-Eliashberg equations (ME) and the Allen-Dynes equation for strongly coupled systems (AD) using $\mu^* = 0.1-0.13$ at 270 GPa. The pressure range where dynamic stability was confirmed in this study (phonon calculations were carried out between 140 and 270 GPa, see Section S2.4, S3.4, and S4.4) is also provided in GPa.

Calculated strong coupling and shape dependence correction factors, f_1 and f_2 , used in the AD equation are: $Im\bar{3}m$ H₃S: $f_1 = 1.067$, $f_2 = 1.022$, $R3m$ H₃S: $f_1 = 1.052$, $f_2 = 1.017$, T_d -CS₃H₁₂: $f_1 = 1.039$, $f_2 = 1.016$, $R3m$ CSH₇: $f_1 = 1.058$, $f_2 = 1.022$, Cm CS₃H₁₃: $f_1 = 1.046$, $f_2 = 1.013$, $R3m$ CS₃H₁₃: $f_1 = 1.047$, $f_2 = 1.019$, Cm CS₇H₂₅: $f_1 = 1.047$, $f_2 = 1.017$.

255 GPa is primarily a result of decreased S-H interaction at lower pressures.

We also considered O_h -CS₅₃H₁₆₂, which corresponds to 1.85% doping, with calculated C-H bond lengths of 1.16 Å and S-H bonds ranging from 1.43 to 1.48 Å. Unsurprisingly, its DOS at E_F of 0.048 states $eV^{-1}A^{-3}$ and its Θ_D of 1368 K approach the values obtained for $Im\bar{3}m$ H₃S (Table 1). Phonon calculations revealed that this phase was dynamically stable at 270 GPa, and it could be stabilized to lower pressures than O_h -CS₁₅H₄₈, becoming unstable by 160 GPa.

The 25% doped CS₃H₁₂ phase with four-coordinate carbon was stable between 160 and 270 GPa and visualization of the largest magnitude imaginary mode found at the R point at 140 GPa illustrated that it corresponded to a symmetric/asymmetric H-S-H stretch. For 12.5% doping three different structures, which could be described by the distribution of the CH₄ units relative to each

other, were considered (Supplementary Fig. 8). The methane molecules could be isolated, or form CH₄ chains or CH₄ sheets, with $Fmm2$, Pm or $Amm2$ symmetries, respectively. At 270 GPa the $Amm2$ structure was more stable by 10/16 meV/atom with respect to $Pm/Fmm2$, suggesting that “phase separation” is preferred. However, $Amm2$ -CS₇H₂₄ became dynamically unstable near 250 GPa, $Fmm2$ at 160 GPa, and Pm at 140 GPa. CS₁₅H₄₈ became dynamically unstable near 160 GPa via a softening of the longitudinal acoustic mode at an off Γ point, and T_d -CS₅₃H₁₆₂ was stable (unstable) at 200 (160) GPa.

C_xS_{1-x}H_{3+x} phases: doping H₃S via Substituting SH₃ by CH₄

Instead of replacing a fraction of the S atoms by C atoms, another way to dope H₃S would be to replace some of the SH₃ units by CH₄ units. Indeed, XRD and equation of state analysis show that the precursor phases of the C-S-H superconductor are (H₂S)₂H₂ and (CH₄)₂H₂ van der Waals compounds that have identical volumes at the synthesis pressure, thereby allowing readily mixed (H₂S,CH₄)₂H₂ alloys¹¹. This leads to the possibility that CH₄ molecules persist well into the superconducting H₃S-based phase or phases with H₂ taken up in the structure. First-principles calculations have previously been employed to investigate the properties of metastable phases that correspond to 50% SH₃ → CH₄ substitution, wherein methane molecules were intercalated in an H₃S framework^{35,36}. Lower dopings could be derived from the T_d -C_xS_{1-x}H_{3+x} phases discussed above by adding a single hydrogen atom to the S-H lattice.

For the 25% and 12.5% CH₄ dopings two different structures were considered; those where CH₄ does not possess any neighbours ($R3m$) and where it forms chains Cm (Supplementary Fig. 13). Unlike structures where C replaced S, the CH₄ dopings we considered (25, 12.5, 6.25, and 1.85% C) were all found to be dynamically stable at 270 GPa and many of them remained stable to at least 140 GPa (Table 1, Supplementary Figs. 14, and 16–17). The Bader charge on the C_{3v} symmetry methane molecule in CS₁₅H₄₉ was nearly the same as in T_d -CS₁₅H₄₈, -0.10, but the bonds were somewhat shorter and stronger (1.03 Å and 6.92 eV/bond ($\times 1$), 1.04 Å and 6.98 eV/bond ($\times 3$)) and the angles were closer to those of a perfect tetrahedron (105°, 113°). The DOS at E_F of CS₁₅H₄₉ (0.034 states $eV^{-1}A^{-3}$) is quite comparable to that of T_d -CS₁₅H₄₈, but its Θ_D is significantly higher (1792 K, Table 1), suggesting that its T_c may be higher as well.

Thermodynamic properties and equation of states

The relative enthalpies of the doped C-S-H structures (Fig. 4) illustrate that doping is thermodynamically unfavorable within the pressure range considered, consistent with previous studies of carbon doped SH₃ phases^{35,36,44}. For a given number of C+S atoms the phase where CH₄ replaced H₃S was always the most stable, followed by phases where a tetrahedrally coordinated C replaced an S atom, and lastly those where C was octahedrally coordinated. Exploratory calculations suggested that it was not enthalpically favorable to add another hydrogen to the SH₃ → CH₄ doped phases by forming an S-H bond (e.g. ΔH for the reaction CS₃H₁₃ + $\frac{1}{2}$ H₂ → CS₃H₁₄ was +17.8 meV/atom).

The enthalpies of the phases with the lowest levels of doping were within < 8 meV/atom of each other, and they were the closest to the threshold for thermodynamic stability, with ΔH for the formation of CS₅₃H₁₆₃ being 0.14 and 6.82 meV/atom at 140 and 270 GPa, respectively. At 270 GPa the zero-point-energy disfavored the doped species where carbon was tetrahedrally coordinated (Supplementary Table 3) but this had less of an effect on the octahedrally coordinated systems, such that for S → C replacements, the structures in which C was six coordinate generally became slightly preferred. Even though the carbon doped phases are not thermodynamically stable, their enthalpies of formation are generally within the ~70 meV/atom threshold

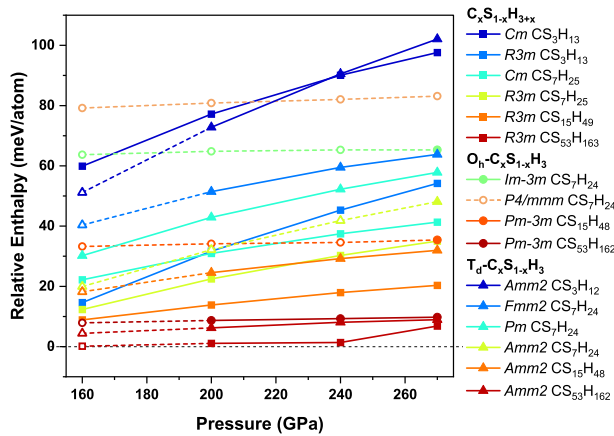


Fig. 4 ΔH as a function of pressure. Formation enthalpies are calculated via the following reaction: $C + x(H_2S) + (\frac{y-3x}{2})H_2 \rightarrow CS_xH_y$ in meV/atom using the diamond phase of carbon⁷³, C2/c phase of H_2 ⁷⁴ and $Im\bar{3}m$ phase of H_2S ¹⁶ as a reference. The open (closed) circles correspond to structures that were found to be dynamically unstable (stable). For a plot of the full enthalpy range see Supplementary Fig. 26.

corresponding to the 90th percentile of DFT-calculated metastability for inorganic crystalline materials at 1 atm⁶¹. Moreover, the increase of configurational entropy upon substituting C or CH_4 into the SH_3 framework will favor the ternary. Statistical analysis of the AFLOW data repository has shown that stability for three or four component systems is typically due to entropic factors⁶².

Superconducting properties

In addition to the phonon band structures and phonon densities of states, we calculated the Eliashberg spectral function, $\alpha^2F(\omega)$, and the EPC integral, $\lambda(\omega)$, for the model structures whose unit cell sizes were small enough so that we could obtain converged results (Supplementary Figs. 8a and 13a–d). In a recent theoretical study the highest T_c calculated for O_h - CS_7H_{24} was 170 K at 250 GPa⁴⁵. Other phases with octahedrally coordinated carbon, but lower doping levels, possessed N_F values that fell below that of $Im\bar{3}m$ H_2S and Θ_{DS} that were only slightly higher than that of $R3m$ H_2S (Table 1), in-line with computations suggesting that their superconducting response is unlikely to surpass that of the undoped binary⁴⁵. Because of this, we did not investigate the superconducting properties of the O_h family of structures.

The two sets of phases with tetrahedrally coordinated carbon atoms possessed N_F values similar to the octahedral family, but their estimated Θ_{DS} were higher. Nonetheless, the logarithmic average frequency, ω_{ln} , of T_d - CS_3H_{12} was lower than that of H_2S resulting in a substantially lower T_c . Even though decreasing the doping increases N_F , once again it is unlikely that compounds belonging to this family of structures could be superconducting at temperatures higher than those found for H_2S . However, adding one more hydrogen atom per unit cell to members of this family leads to a remarkable improvement. Both ω_{ln} and λ of CS_3H_{13} are higher than that of T_d - CS_3H_{12} , yielding a T_c up to 142 K at 270 GPa.

To better understand how adding a single hydrogen atom can dramatically increase T_c by 60 K, we compare $\lambda(\omega)$ and $\omega_{ln}(\omega)$ of these two model structures (Supplementary Fig. 22). At ~ 1550 cm^{-1} their $\omega_{ln}(\omega)$ are almost identical. At higher frequencies $\omega_{ln}(\omega)$ for CS_3H_{13} increases much faster until a near plateau region is attained at 2220 cm^{-1} (1670 K). In T_d - CS_3H_{12} , on the other hand, $\omega_{ln}(\omega)$ reaches 1309 K at 2450 cm^{-1} . Beyond ~ 2500 cm^{-1} , the flat high-frequency bands contribute less than 40 K to $\omega_{ln}(\omega)$ for both structures. Therefore, the main difference in the total ω_{ln} for the two phases arises from modes in the

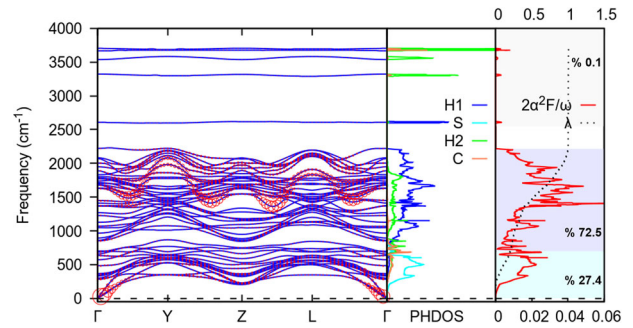


Fig. 5 Superconducting properties of $CmCS_3H_{13}$. Phonon band structure, phonon density of states (PHDOS), Eliashberg spectral function in the form of $\frac{2\alpha^2F(\omega)}{\omega}$, and the electron phonon integral, $\lambda(\omega)$, for $CmCS_3H_{13}$ at 270 GPa. Red circles indicate the electron-phonon coupling constant, λ_{qv} , at mode ν and wavevector \mathbf{q} , and their radii are proportional to the strength. H1 are the hydrogen atoms in the S-H lattice, and H2 are the hydrogen atoms in CH_4 . The percentages given were calculated via $(\int_{\omega_1}^{\omega_2} \lambda(\omega)d\omega/\lambda) \times 100\%$; and the frequency regions spanning ω_1 and ω_2 are color coded in the PHDOS.

1550–2500 cm^{-1} frequency range. From the projected phonon density of states (Supplementary Fig. 24) modes associated with motions of the H atoms in the H-S lattice (H1) primarily comprise this region, with some contribution from H atoms in the CH_4 molecule (H2). At ~ 1410 cm^{-1} $\lambda(\omega)$ was almost the same for the two structures (~ 0.45). At higher frequencies the $\lambda(\omega)$ for CS_3H_{13} increases much faster until 2220 cm^{-1} where it reaches a value of 1.00, while for T_d - CS_3H_{12} $\lambda(\omega)$ reaches 0.83 at 2450 cm^{-1} . Beyond ~ 2500 cm^{-1} , the high-frequency flat bands contribute less than 0.005 towards λ for both structures.

Additional insight into the types of motions that result in a larger λ within CS_3H_{13} can be obtained by visualizing selected vibrational modes that have a notable λ_{qv} , e.g., modes about halfway along the $Y \rightarrow Z$ (1412 cm^{-1}) and $Z \rightarrow L$ (1361 cm^{-1}) paths, which have very large contributions (Fig. 5). Both of these involve H2 vibrations between neighboring S atoms, leading to a snakelike undulation of the H1/H2 chains. The addition of the extra S-bonded H atom expands the S-H lattice in the ab plane, leaving looser contacts between the S and H atoms (1.44 Å and 1.43 Å as opposed to 1.41–1.43 Å in T_d - CS_3H_{12}), thereby softening the phonon frequencies. The c axis is largely unchanged by the addition of an extra H, but the H–S distances that are relatively even in CS_3H_{12} (1.43–1.44 Å) become disproportionate in CS_3H_{13} to 1.41 and 1.46 Å. Within the methane fragments, two H1 atoms possessed mirrored circular motions that were part of the undulating H chains.

Notably, the T_c of $R3mCS_3H_{13}$ is ~ 20 –30 K lower than that of the Cm symmetry structure even though the N_F and λ of both is approximately the same. Our analysis (Supplementary Discussion 4) illustrates the main reason for this difference arises from the increased ω_{ln} of the Cm phase, which again is a result of the aforementioned snakelike undulations of the H1/H2 chains. The H-S distances in the Cm phase are more even (Supplementary Fig. 13) than in $R3m$, which possesses some S-H-S contacts that are beginning to disproportionate. Comparison of the results obtained for $R3mCS_7H_{25}$ and $CmCS_7H_{25}$ shows that N_F does not necessarily correlate with λ . However, analysis of the $\lambda(\omega)$ plots (Supplementary Fig. 23) of all of the phases considered show they begin to deviate near 1300 cm^{-1} with the contributions in this intermediate frequency regime being key for increasing λ . Using the ω_{ln} , f_1 and f_2 parameters obtained for $CmCS_3H_{13}$ we find that a $\lambda = 2.25$ yields $T_c = 280$ K via the Allen-Dynes modified McMillan equation. Within the Eliashberg formalism, somewhat smaller λ values would yield a similar result. Given that $\lambda = 2.19$ for $Im\bar{3}mH_2S$ at

200 GPa¹⁷, it is plausible that a C–S–H phase possessing a similar EPC, but significantly larger ω_{in} could be found by maximizing the Eliashberg spectral function between ~ 1300 and 2500 cm^{-1} .

In summary, our detailed computations have shown that doping H₃S by 1.85–25% carbon at 270 GPa leads to a plethora of metastable phases where carbon can be either six-coordinated or four-coordinated to hydrogen. In the first case we see the remarkable emergence of an O_h symmetry CH₆ motif reminiscent of a di-carbocation, but stabilized in the solid state under pressure via weak interactions by the negatively charged environment of the surrounding host H₃S-like lattice. The second case is an example of methane intercalated within an H₃S-like framework. These doping schemes split degenerate bands thereby decreasing N_F , and localizing electrons in covalent C–H bonds whose signatures are far removed from the Fermi energy.

The ω_{in} and λ of $T_d\text{-CS}_3\text{H}_{12}$ were smaller than the values computed for $Im\bar{3}m$ H₃S, as was the resulting T_c . Remarkably, adding a single hydrogen atom to $T_d\text{-CS}_3\text{H}_{12}$ increased T_c by 60 K. The larger λ and ω_{in} of the resulting CS₃H₁₃ phase could be traced back to the emergence of soft phonon modes, a consequence of the weaker and longer S–H bonds in the host lattice caused by the insertion of the extra S-bonded hydrogen atom. At 270 GPa the T_c of CS₃H₁₃ was about the same as that of $R\bar{3}m$ H₃S despite its much lower DOS at E_F . At this pressure the predicted T_c s of the metastable phases considered here spanned ~ 80 K, a variation that depends on the coordination of the carbon and the hydrogen stoichiometry. We hope that the present results will stimulate further theoretical studies, large supercell calculations of the superconducting properties of these structures, as well as additional experiments in search of still higher T_c s and phases that may be stable over a broader range of conditions.

METHODS

Electronic structure calculations

Geometry optimizations and electronic structure calculations were performed using density functional theory (DFT) with the Perdew–Burke–Ernzerhof (PBE) exchange correlation functional⁶³ as implemented in the Vienna Ab initio Simulation Package (VASP) 5.4.1⁶⁴. The valence electrons (H 1s¹, S 3s²3p⁴, and C 2s²2p²) were treated explicitly using plane wave basis sets with a cutoff energy of 800 eV (as previously employed by Cui et al.³⁵), while the core states were treated with the projector-augmented wave (PAW)⁶⁵ method. The reciprocal space was sampled using a Γ -centered Monkhorst–Pack scheme, and the number of divisions along each reciprocal lattice vector was chosen such that the product of this number with the real lattice constant was 70 Å for the density of states (DOS) calculations, and 50 Å otherwise. The crystal orbital Hamilton populations (COHPs)⁶⁶, the negative of the COHPs integrated to the Fermi level (–iCOHPs), and the crystal orbital bond index (COBI)⁴⁶ were calculated using the LOBSTER package (v2.2.1 for –iCOHP and v4.1.0 for COBI)⁶⁷, and the results used to analyze the bonding. The dynamic stability of the phases was investigated via phonon calculations performed using the finite difference scheme as implemented in the PHONOPY software package⁶⁸. For the DFT–raMO procedure⁴⁷, single point calculations were carried out in VASP with coarse k -point grids sampling the full Brillouin zone with dimensions equal to the supercell used in the raMO analysis, corresponding to $3 \times 3 \times 3$ for CS₁₅H₄₈ and $5 \times 5 \times 5$ for H₃S.

Superconducting properties

Phonon calculations were performed using the Quantum Espresso (QE)⁶⁹ program to obtain the dynamical matrix and the electron–phonon coupling (EPC) parameters. The pseudopotentials were obtained from the PSLibrary⁷⁰ using H 1s¹, S 3s²3p⁴, and C 2s²2p² valence electrons and the PBE exchange–correlation functional⁶³. Plane-wave basis set cutoff energies were set to 80 Ry for all systems. We employed a Γ -centered Monkhorst–Pack Brillouin zone sampling scheme, along with Methfessel–Paxton smearing with a broadening width of 0.02 Ry. Density functional

perturbation theory as implemented in QE was employed for the phonon calculations. The EPC matrix elements were calculated using the k and q -meshes, and Gaussian broadenings listed in Supplementary Table 1. The EPC parameter (λ) converges to within 0.05 for differences of the Gaussian broadening that are less than 0.02 Ry. Here, the critical superconducting temperature, T_c , has been estimated using the Allen–Dynes equation, $T_c = \frac{f_1 f_2 \omega_{\text{in}}}{1.2} \exp\left[-\frac{1.04(1+\lambda)}{\lambda - \mu^* (1+0.62\lambda)}\right]$, where ω_{in} is the logarithmic average frequency, μ^* was set to 0.1–0.13 and the f_1 and f_2 correction factors for strong coupling and shape dependence are functions of ω , λ , and μ^* (equaling unity for the weak coupling limit, see Ref. ⁷¹). The T_c s were also obtained by solving the Eliashberg equations⁷² numerically based on the spectral function, $a^2F(\omega)$, obtained from the QE calculations. The Debye temperature in Table 1 was obtained using the PHONOPY software package⁶⁸, as described in the computational details in Supplementary Methods.

DATA AVAILABILITY

The datasets generated during and/or analyzed during the current study are summarized in the Supplementary Information, and are available from the corresponding author on reasonable request.

Received: 27 October 2021; Accepted: 20 March 2022;

Published online: 27 April 2022

REFERENCES

- Ashcroft, N. W. Hydrogen dominant metallic alloys: high temperature superconductors? *Phys. Rev. Lett.* **92**, 187002 (2004).
- Zurek, E., Hoffmann, R., Ashcroft, N. W., Oganov, A. R. & Lyakhov, A. O. A little bit of lithium does a lot for hydrogen. *Proc. Natl Acad. Sci. USA* **106**, 17640–17643 (2009).
- Zurek, E. & Bi, T. High-temperature superconductivity in alkaline and rare earth polyhydrides at high pressure: a theoretical perspective. *J. Chem. Phys.* **150**, 050901 (2019).
- Bi, T., Zarifi, N., Terpstra, T. & Zurek, E. *The search for superconductivity in high pressure hydrides* in Elsevier Reference Module in Chemistry, Molecular Sciences and Chemical Engineering 1–36 (Elsevier, Waltham, MA, 2019).
- Flores-Livas, J. A. et al. A perspective on conventional high-temperature superconductors at high pressure: Methods and materials. *Phys. Rep.* **856**, 1–78 (2020).
- Drozdov, A. P., Erements, M. I., Troyan, I. A., Ksenofontov, V. & Shylin, S. I. Conventional superconductivity at 203 kelvin at high pressures in the sulfur hydride system. *Nature* **525**, 73–76 (2015).
- Somayazulu, M. et al. Evidence for superconductivity above 260 K in lanthanum superhydride at megabar pressures. *Phys. Rev. Lett.* **122**, 027001 (2019).
- Drozdov, A. P. et al. Superconductivity at 250 K in lanthanum hydride under high pressures. *Nature* **569**, 528–531 (2019).
- Snider, E. et al. Room-temperature superconductivity in a carbonaceous sulfur hydride. *Nature* **586**, 373–377 (2020).
- Bykova, E. et al. Structure and composition of C–S–H compounds up to 143 GPa. *Phys. Rev. B* **103**, L14015 (2021).
- Lamichhane, A. et al. X-ray diffraction and equation of state of the C–S–H room-temperature superconductor. *J. Chem. Phys.* **155**, 114703 (2021).
- Goncharov, A. F. et al. Synthesis and structure of carbon-doped H₃S compounds at high pressure. *J. Appl. Phys.* **131**, 025902 (2022).
- Smith, G. A. et al. Lower pressure phases and metastable states of superconducting photoinduced carbonaceous sulfur hydride. arXiv Preprint at <https://arxiv.org/abs/2111.15051> (2021).
- Yao, Y. & Tse, J. S. Superconducting hydrogen sulfide. *Chem. Eur. J.* **24**, 1769–1778 (2017).
- Strobel, T. A., Ganesh, P., Somayazulu, M., Kent, P. R. C. & Hemley, R. J. Novel cooperative interactions and structural ordering in H₂S–H₂. *Phys. Rev. Lett.* **107**, 255503 (2011).
- Li, Y., Hao, J., Liu, H., Li, Y. & Ma, Y. The metallization and superconductivity of dense hydrogen sulfide. *J. Chem. Phys.* **140**, 174712 (2014).
- Duan, D. et al. Pressure-induced metallization of dense (H₂S)₂H₂ with high- T_c superconductivity. *Sci. Rep.* **4**, 6968 (2014).
- Einaga, M. et al. Crystal structure of 200 K-superconducting phase of sulfur hydride system. *Nat. Phys.* **12**, 835–838 (2016).
- Minkov, V. S., Prakash, V. B., Greenberg, E. & Erements, M. I. A boosted critical temperature of 166 K in superconducting D₃S synthesized from elemental sulfur and hydrogen. *Angew. Chem. Int. Ed.* **59**, 38970–18974 (2020).

20. Guigue, B., Marizy, A. & Loubeyre, P. Direct synthesis of pure H₂S from S and H elements: No evidence of the cubic superconducting phase up to 160 GPa. *Rev. B* **95**, 020104(R) (2017).
21. Goncharov, A. F. et al. Hydrogen sulfide at high pressure: change in stoichiometry. *Phys. Rev. B* **93**, 174105 (2016).
22. Laniel, D. et al. Novel sulfur hydrides synthesized at extreme conditions. *Phys. Rev. B* **102**, 134109 (2020).
23. Akashi, R., Kawamura, M., Tsuneyuki, S., Nomura, Y. & Arita, R. First-principles study of the pressure and crystal-structure dependences of the superconducting transition temperature in compressed sulfur hydrides. *Phys. Rev. B* **91**, 224513 (2015).
24. Errea, I. et al. Hydrogen sulphide at high pressure: a strongly-anharmonic phonon-mediated superconductor. *Phys. Rev. Lett.* **114**, 157004 (2015).
25. Li, Y. et al. Dissociation products and structures of solid H₂S at strong compression. *Phys. Rev. B* **93**, 020103(R) (2016).
26. Ishikawa, T. et al. Superconducting H₂S₂ phase in sulfur-hydrogen system under high-pressure. *Sci. Rep.* **6**, 23160 (2016).
27. Akashi, R., Sano, W., Arita, R. & Tsuneyuki, S. Possible “Magneli” phases and self-alloying in the superconducting sulfur hydride. *Phys. Rev. Lett.* **117**, 075503 (2016).
28. Gordon, E. E. et al. Structure and composition of the 200 K-superconducting phase of H₂S at ultrahigh pressure: the perovskite (SH⁻)(H₃S⁺). *Angew. Chem. Int. Ed.* **55**, 3682–3684 (2016).
29. Majumdar, A., Tse, J. S. & Yao, Y. Modulated structure calculated for superconducting hydrogen sulfide. *Angew. Chem. Int. Ed.* **56**, 11390–11393 (2017).
30. Majumdar, A., Tse, J. S. & Yao, Y. Mechanism for the structural transformation to the modulated superconducting phase of compressed hydrogen sulfide. *Sci. Rep.* **9**, 5023 (2019).
31. Verma, A. K. & Modak, P. A unique metallic phase of H₂S at high-pressure: sulfur in three different local environments. *Phys. Chem. Chem. Phys.* **20**, 26344–26350 (2018).
32. Errea, I. et al. Quantum hydrogen-bond symmetrization in the superconducting hydrogen sulfide system. *Nature* **532**, 81–84 (2016).
33. Bianco, R., Errea, I., Calandra, M. & Mauri, F. High-pressure phase diagram of hydrogen and deuterium sulfides from first principles: structural and vibrational properties including quantum and anharmonic effects. *Phys. Rev. B* **97**, 214101 (2018).
34. Liu, C. et al. Strain-induced modulations of electronic structure and electron-phonon coupling in dense H₂S. *Phys. Chem. Chem. Phys.* **20**, 5952–5957 (2018).
35. Cui, W. et al. Route to high-T_c superconductivity via CH₄ intercalated H₂S hydride perovskites. *Phys. Rev. B* **101**, 134504 (2020).
36. Sun, Y. et al. Computational discovery of a dynamically stable cubic SH₃-like high-temperature superconductor at 100 GPa via CH₄ intercalation. *Phys. Rev. B* **101**, 174102 (2020).
37. Gubler, M., Flores-Livas, J. A., Kozhevnikov, A. & Goedecker, S. Missing theoretical evidence for conventional room-temperature superconductivity in low-enthalpy structures of carbonaceous sulfur hydrides. *Phys. Rev. Mater.* **6**, 014801 (2022).
38. Du, M., Zhang, Z., Cui, T. & Duan, D. Pressure-induced superconducting CS₂H₁₀ with an H₂S framework. *Phys. Chem. Chem. Phys.* **23**, 22779–22784 (2021).
39. Ge, Y., Zhang, F., Dias, R. P., Hemley, R. J. & Yao, Y. Hole-doped room-temperature superconductivity in H₃S_{1-x}Z_x (Z=C, Si). *Mater. Today Phys.* **15**, 100330 (2020).
40. Quan, Y. & Pickett, W. E. Van Hove singularities and spectral smearing in high-temperature superconducting H₂S. *Phys. Rev. B* **93**, 104526 (2016).
41. Sano, W., Koretsune, T., Tadano, T., Akashi, R. & Arita, R. Effect of van Hove singularities on high-T_c superconductivity in H₂S. *Phys. Rev. B* **93**, 094525 (2016).
42. Ortenzi, L., Cappelluti, E. & Pietronero, L. Band structure and electron-phonon coupling in H₂S: A tight-binding model. *Phys. Rev. B* **94**, 064507 (2016).
43. Akashi, R. Archetypical “push the band critical point” mechanism for peaking of the density of states in three dimensional crystals: theory and case study of cubic H₂S. *Phys. Rev. B* **101**, 075126 (2020).
44. Wang, T. et al. Absence of conventional room-temperature superconductivity at high pressure in carbon-doped H₂S. *Phys. Rev. B* **104**, 064510 (2021).
45. Guan, H., Sun, Y. & Liu, H. Superconductivity of H₂S doped with light elements. *Phys. Rev. Res.* **3**, 043102 (2021).
46. Müller, P. C., Ertural, C., Hempelmann, J. & Dronskowski, R. Crystal orbital bond index: covalent bond orders in solids. *J. Phys. Chem. C* **125**, 7959–7970 (2021).
47. Yannello, V. J., Lu, E. & Fredrickson, D. C. At the limits of isolobal bonding: π -based covalent magnetism in Mn₂Hg₅. *Inorg. Chem.* **59**, 12304–12313 (2020).
48. Hoffmann, R. The theoretical design of novel stabilized systems. *Pure Appl. Chem.* **28**, 181–194 (1971).
49. Hoffmann, R., Alder, R. W. & Wilcox Jr, C. F. Planar tetracoordinate carbon. *J. Am. Chem. Soc.* **92**, 4992–4993 (1970).
50. Olah, G. A. & Rasul, G. From kekulé’s tetravalent methane to five-, six-, and seven-coordinated protonated methanes. *Acc. Chem. Res.* **30**, 245–250 (1997).
51. Olah, G. A., Prakash, G. K. S., Williams, R. E., Field, L. D. & Wade, K. (eds) *Hypercarbon Chemistry* (John Wiley & Sons, New York, 1987).
52. Fahy, S. & Louie, S. G. High-pressure structural and electronic properties of carbon. *Phys. Rev. B* **36**, 36 (1987).
53. Martínez-Canales, M. & Pickard, C. J. Thermodynamically stable phases of carbon at multiterapascal pressures. *Phys. Rev. Lett.* **108**, 045704 (2012).
54. Daviau, K. & Lee, K. M. Zinc-blende to rocksalt transition in SiC in a laser-heated diamond-anvil cell. *Phys. Rev. B* **95**, 134108 (2017).
55. Hatch, D. M. et al. Bilayer sliding mechanism for the zinc-blende to rocksalt transition in SiC. *Phys. Rev. B* **71**, 184109 (2005).
56. Gao, G., Liang, X., Ashcroft, N. W. & Hoffmann, R. Potential semiconducting and superconducting metastable Si₃C structures under pressure. *Chem. Mater.* **30**, 421 (2018).
57. Marx, D. & Parrinello, M. Structural quantum effects and three-centre two-electron bonding in CH₃⁺. *Nature* **375**, 216–218 (1995).
58. Lammertsma, K. & Olah, G. A. Diprotonated methane, CH₆²⁺, and diprotonated ethane, C₂H₆²⁺. *J. Am. Chem. Soc.* **104**, 6851–6852 (1982).
59. Lammertsma, K. et al. Structure and stability of diprotonated methane, CH₆²⁺. *J. Am. Chem. Soc.* **105**, 5258–5263 (1983).
60. Feng, J. et al. Structures and potential superconductivity in SiH₄ at high pressure: En route to “metallic hydrogen”. *Phys. Rev. Lett.* **96**, 017006 (2006).
61. Sun, W. et al. The thermodynamic scale of inorganic crystalline metastability. *Sci. Adv.* **2**, e1600225 (2016).
62. Toher, C., Oses, C., Hicks, D. & Curtarolo, S. Unavoidable disorder and entropy in multicomponent systems. *npj Comput. Mater.* **5**, 69 (2019).
63. Perdew, J. P., Burke, K. & Ernzerhof, M. Generalized gradient approximation made simple. *Phys. Rev. Lett.* **77**, 3865 (1996).
64. Kresse, G. & Furthmüller, J. Efficient iterative schemes for ab initio total-energy calculations using a plane-wave basis set. *Phys. Rev. B* **54**, 11169 (1996).
65. Blöchl, P. E. Projector augmented-wave method. *Phys. Rev. B* **50**, 17953 (1994).
66. Dronskowski, R. & Blöchl, P. E. Crystal orbital hamilton populations (COHP): Energy-resolved visualization of chemical bonding in solids based on density-functional calculations. *J. Phys. Chem.* **97**, 8617–8624 (1993).
67. Maintz, S., Deringer, V. L., Tchougréeff, A. L. & Dronskowski, R. Analytic projection from plane-wave and PAW wavefunctions and application to chemical-bonding analysis in solids. *J. Comput. Chem.* **34**, 2557–2567 (2013).
68. Togo, A., Oba, F. & Tanaka, I. First-principles calculations of the ferroelastic transition between rutile-type and CaCl₂-type SiO₂ at high pressures. *Phys. Rev. B* **78**, 134106 (2008).
69. Giannozzi, P. et al. Quantum espresso: a modular and open-source software project for quantum simulations of materials. *J. Phys. Condens. Matter* **21**, 395502 (2009).
70. Dal Corso, A. Pseudopotentials periodic table: From H to Pu. *Comput. Mater. Sci.* **95**, 337–350 (2014).
71. Allen, P. B. & Dynes, R. C. Transition temperature of strong-coupled superconductors reanalyzed. *Phys. Rev. B* **12**, 905 (1975).
72. Eliashberg, G. M. Interactions between electrons and lattice vibrations in a superconductor. *Sov. Phys. JETP* **11**, 696–702 (1960).
73. Martínez-Canales, M., Pickard, C. J. & Needs, R. J. Thermodynamically stable phases of carbon at multiterapascal pressures. *Phys. Rev. Lett.* **108**, 045704 (2012).
74. Liu, H., Zhu, L., Cui, W. & Ma, Y. Room-temperature structures of solid hydrogen at high pressures. *J. Chem. Phys.* **137**, 074501 (2012).

ACKNOWLEDGEMENTS

We are grateful to R. Hoffmann, G.W. Collins, and R.P. Dias for useful discussions. We acknowledge support from the U.S. National Science Foundation (DMR-1827815 to E.Z. and DMR-1933622 to R.J.H.). This research was also supported by the U.S. Department of Energy (DOE), Office of Science, Fusion Energy Sciences under Award No. DE-SC0020340 and DOE, National Nuclear Security Administration, through the Chicago/DOE Alliance Center under Cooperative Agreement Grant No. DE-NA0003975. Computations were carried out at the Center for Computational Research at the University at Buffalo (<http://hdl.handle.net/10477/79221>).

AUTHOR CONTRIBUTIONS

R.J.H. and E.Z. conceived the project. X.W., T.B., K.P.H., and A.L. carried out the DFT calculations. All authors were involved in data analysis and results discussions. X.W., E.Z. and R.J.H. wrote the manuscript, with contributions from K.P.H.

COMPETING INTERESTS

The authors declare no competing interests.

ADDITIONAL INFORMATION

Supplementary information The online version contains supplementary material available at <https://doi.org/10.1038/s41524-022-00769-9>.

Correspondence and requests for materials should be addressed to Russell J. Hemley or Eva Zurek.

Reprints and permission information is available at <http://www.nature.com/reprints>

Publisher's note Springer Nature remains neutral with regard to jurisdictional claims in published maps and institutional affiliations.



Open Access This article is licensed under a Creative Commons Attribution 4.0 International License, which permits use, sharing, adaptation, distribution and reproduction in any medium or format, as long as you give appropriate credit to the original author(s) and the source, provide a link to the Creative Commons license, and indicate if changes were made. The images or other third party material in this article are included in the article's Creative Commons license, unless indicated otherwise in a credit line to the material. If material is not included in the article's Creative Commons license and your intended use is not permitted by statutory regulation or exceeds the permitted use, you will need to obtain permission directly from the copyright holder. To view a copy of this license, visit <http://creativecommons.org/licenses/by/4.0/>.

© The Author(s) 2022